

Soft MeV Gamma-Ray Background from Low-Luminosity Active Galactic Nuclei and Connection to the Origin of IceCube PeV Neutrinos

Shigeo S. Kimura,^{1, 2, 3, 4, 5} Kohta Murase,^{3, 4, 5, 6} and Peter Mészáros^{3, 4, 5}

¹*Frontier Research Institute for Interdisciplinary Sciences, Tohoku University, Sendai 980-8578, Japan*

²*Astronomical Institute, Tohoku University, Sendai 980-8578, Japan*

³*Department of Physics, The Pennsylvania State University, University Park, Pennsylvania 16802, USA*

⁴*Department of Astronomy & Astrophysics, The Pennsylvania State University, University Park, Pennsylvania 16802, USA*

⁵*Center for Particle and Gravitational Astrophysics,*

The Pennsylvania State University, University Park, Pennsylvania 16802, USA

⁶*Yukawa Institute for Theoretical Physics, Kyoto, Kyoto 606-8502 Japan*

(Dated: May 6, 2020)

Low-luminosity active galactic nuclei (LL AGNs) have radiatively inefficient accretion flows (RIAFs), where thermal electrons naturally emit not only synchrotron photons but also soft gamma rays via the Comptonization of their synchrotron photons. We find that without any nonthermal electron population, these upscattered photons from LL AGNs naturally account for the MeV gamma-ray background, whose origin has been a mystery. The model also allows proton acceleration via turbulence or reconnections, producing high-energy neutrinos via hadronuclear interactions. We demonstrate that our RIAF model can simultaneously reproduce the soft (MeV) gamma-ray and high-energy (PeV) neutrino backgrounds. The proposed model is consistent with the latest x-ray observations of nearby LL AGNs and testable by future MeV gamma-ray telescopes.

INTRODUCTION

The Universe is filled with high-energy radiation, including x rays [1], gamma rays [2, 3], and high-energy neutrinos [4–8]. It is widely believed that the bulk of the cosmic x-ray background is produced by radio-quiet active galactic nuclei (AGNs) [9], while radio-loud AGNs including blazars predominantly contribute to the extragalactic gamma-ray background in the GeV-TeV range [10].

The origin of the soft gamma-ray background has yet to be determined (see Ref. [11] for a review). Although type Ia supernovae [12, 13], radio galaxies [14] including flat-spectrum radio quasars (FSRQ; [15]), and dark matter [16, 17] were proposed, recent works indicate that these candidates cannot explain all of the measured intensity with standard parameters [18–22]. Alternatively, Refs. [23–25] suggested that nonthermal electrons accelerated in the coronae in radio-quiet AGNs can account for the MeV gamma-ray background. However, the existence of nonthermal electrons is highly speculative because the electrons are rapidly thermalized by Coulomb collisions in typical coronae [26]. On the other hand, proton acceleration by reconnections and turbulence may naturally occur due to their slower Coulomb relaxation, in which hadronic gamma rays are unavoidable through proton-induced electromagnetic cascades inside the magnetized coronae. In this hadronic scenario, RQ AGNs including Seyfert galaxies and quasars can explain the high-energy neutrino background in the 10–100 TeV range, which predicts that $\sim 20 - 100\%$ of the observed MeV gamma-ray background should be accounted for [26].

We here propose a scenario to naturally explain the soft gamma-ray background in the MeV range without

relying on nonthermal mechanisms. Radiatively inefficient accretion flows (RIAFs; [27–29]) are ubiquitously expected in low-luminosity AGNs (LL AGNs), and observed infrared and radio emissions are explained by synchrotron radiation from hot thermal electrons. We show that associated soft gamma rays from the Comptonization naturally make a significant contribution to the gamma-ray background up to ~ 10 MeV. In addition, protons in the RIAFs can be accelerated and efficiently emit neutrinos via hadronic interactions [30–34], which implies that our RIAF model can naturally account for the current gamma-ray and neutrino backgrounds simultaneously. We use the notation $Q_X = Q/10^X$ in cgs units, and ε_i (E_i) for the source-frame (observer-frame) energy of particle i unless otherwise noted.

GUARANTEED SOFT GAMMA RAYS FROM RIAFS

First we provide basic properties of standard RIAFs (see the accompanying paper [35] for technical details). We consider an accreting plasma of size R around a supermassive black hole (SMBH) of mass M_{BH} with an accretion rate \dot{M} . We use the normalized radius and mass accretion rate, $\mathcal{R} = R/R_S$ and $\dot{m} = \dot{M}c^2/L_{\text{Edd}}$, respectively, where R_S is the Schwarzschild radius and L_{Edd} is the Eddington luminosity. Based on recent numerical simulations (e.g., Refs. [36–41]), the radial velocity, number density, and magnetic field in the RIAF are analytically approximated to be $V_R \approx \alpha V_K/2 \simeq 3.4 \times 10^8 \mathcal{R}_1^{-1/2} \alpha_{-1} \text{ cm s}^{-1}$, $n_p \approx \dot{M}/(4\pi m_p R H V_R) \simeq 4.6 \times 10^8 \mathcal{R}_1^{-3/2} \alpha_{-1}^{-1} M_8^{-1} \dot{m}_{-2} \text{ cm}^{-3}$, and $B \approx \sqrt{8\pi n_p k_B T_p/\beta} \simeq 2.1 \times 10^2 \mathcal{R}_1^{-5/4} \alpha_{-1}^{-1/2} M_8^{-1/2} \dot{m}_{-2}^{1/2} \beta_{-1}^{-1/2}$

TABLE I. Parameters and resulting quantities in our models.

Model parameters						
α	β	\mathcal{R}	$\eta_{\text{rad, sd}}$	$M_{\text{BH}}/\text{M}_\odot$	$\kappa_{\text{bol}/X}$	$\kappa_{X/\text{H}\alpha}$
0.1	10	10	0.1	1×10^8	15	6.0
Resulting quantities for various $L_{X,\text{obs}}$						
$\log L_{X,\text{obs}}$	$\log \dot{m}$	τ_T	Θ_e	$\log E_{\gamma\gamma}$	$P_{\text{CR}}/P_{\text{th}}$	
[erg s $^{-1}$]				[MeV]	[%]	
38.78	-3.33	-2.38	3.38	5.58	1.5	
39.68	-2.88	-1.93	2.74	5.24	1.4	
40.59	-2.43	-1.48	2.08	4.16	1.2	
41.50	-1.98	-1.02	1.49	3.44	0.88	
42.40	-1.52	-0.57	1.05	2.25	0.57	

G , where α is the viscosity parameter [42], $V_K = \sqrt{GM/R}$ is the Keplerian velocity, $k_B T_p \approx GM_{\text{BH}} m_p/(2R) \simeq 23 \mathcal{R}_1$ MeV is the proton temperature, and $\beta = P_{\text{th}}/P_B$ is the plasma beta. Observations of x-ray binaries and AGNs demand $\alpha \sim 0.1 - 1$ [43], while the global MHD simulations result in $\alpha \sim 0.01 - 0.1$ and $\beta \sim 3 - 30$ [38, 44]. Hence, we set $\alpha = 0.1$ and $\beta = 10$ as their reference values.

In the RIAFs, photons are mainly created by thermal electrons through synchrotron radiation, bremsstrahlung, and inverse Compton scattering. We calculate the photon spectra by the method in Ref. [30]. The electron temperature is determined so that the resulting photon luminosity is equal to the bolometric luminosity estimated by \dot{m} . Assuming that Coulomb collisions are the dominant heating process for the electrons, we write a relation between \dot{m} and bolometric luminosity, L_{bol} , as $L_{\text{bol}} \approx \eta_{\text{rad, sd}} \dot{m}_{\text{crit}} L_{\text{Edd}} (\dot{m}/\dot{m}_{\text{crit}})^2$, where $\eta_{\text{rad, sd}} \sim 0.1$ is the radiation efficiency for the standard disk [45], and $\dot{m}_{\text{crit}} \approx 0.03 \alpha_{-1}^2$ is the critical mass accretion rate above which the RIAF no longer exists [46–49]. Note that this treatment is qualitatively different from the previous work [30] where $L_{\text{bol}} \propto \dot{m}$ is assumed. Such a treatment may be appropriate if the electrons are directly heated by the plasma dissipation process [50–53]. But these details will not change our conclusions on LL AGNs bright in soft MeV gamma rays. The observed x-ray luminosity at the 2–10 keV band can be converted to the bolometric luminosity using the bolometric correction factor, $\kappa_{\text{bol}/X} = L_{\text{bol}}/L_{X,\text{obs}} \simeq 15$ for LL AGNs [54–57]. We provide $L_{X,\text{obs}}$ as a primary parameter and convert it to \dot{m} using $\kappa_{\text{bol}/X}$ and the relation between \dot{m} and L_{bol} .

For parameter sets shown in Table I, the values of the physical quantities, including the electron temperature, $\Theta_e = k_B T_e/(m_e c^2)$, and the Thomson optical depth, $\tau_T \approx 0.095 M_8^{-1} \mathcal{R}_1 \dot{m}_{-2} \alpha_{-1}^{-1}$, are tabulated in Table I. The resulting x-ray luminosity matches $L_{X,\text{obs}}$ within a factor of 2, although our method does not guarantee it. The RIAFs become optically thick to synchrotron self-absorption, and the absorp-

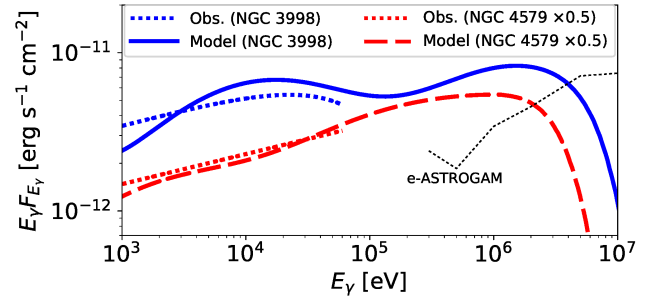


FIG. 1. Thermal photon spectra from the RIAFs in NGC 3998 (blue-solid) and NGC 4579 (red-dashed). The thick-dotted lines are the best-fit curves of x-ray observations. We use $\kappa_{\text{bol}/X} = 9$ for NGC 3998 to match the normalization to the observed value. The thin-dotted line is the sensitivity curve of e-ASTROGAM with 1-yr integration [58].

tion frequency located at the radio band is higher than the value derived from the optically thin limit. In this case, the absorption frequency is determined such that the synchrotron emissivity equals to the black-body radiation: $\varepsilon_{\text{syn}} \approx 3\pi x_M h_p e B \Theta_e^2 / (4\pi m_e c) \simeq 0.005 B_2 \Theta_{e,0}^2 x_{M,3}$ eV, where $x_M \sim 10^3$ represents the discrepancy of the absorption frequency between the optically thin and thick limits [48]. The synchrotron luminosity from an optically thick source is represented by $L_{\text{syn}} \approx \pi (2\varepsilon_{\text{syn}}^3 k_B T_e / [h_p^3 c^2]) \pi R^2 \simeq 3.6 \times 10^{39} \text{ erg s}^{-1} M_8^2 \mathcal{R}_1^2 \Theta_{e,0}^7 B_2^3 x_{M,3}^3$.

The thermal electrons up-scatter the synchrotron photons, and the resulting spectrum can be approximated to be a power-law form with the index of $\alpha_{\text{IC}} = -\ln \tau_T / \ln A_{\text{IC}}$, where $A_{\text{IC}} = 4\Theta_e + 16\Theta_e^2$ [59]. If $\alpha_{\text{IC}} < 1$, the Comptonization dominates over the other cooling processes. For $\Theta_e \sim 2$, the condition is satisfied as long as $\tau_T \gtrsim 0.014$, i.e., $\dot{m} \gtrsim 3 \times 10^{-3}$ (see Table I). The luminosity of the Comptonized photons can be given by $L_{\text{IC}} \approx L_{\text{syn}} (3k_B T_e / \varepsilon_{\text{syn}})^{1-\alpha_{\text{IC}}}$. Owing to the strong Θ_e dependence, our model predicts that electron temperature in the RIAF lies in a narrow range of $\Theta_e \sim 1-3$, unavoidably making a peak at the MeV range for $\dot{m} \gtrsim 3 \times 10^{-3}$ (see Refs. [30, 35] and Supplemental Material for the complete spectra).

Our model is consistent with high-energy observations of nearby LL AGNs. Recently, Ref. [60] reported an estimate of the electron temperature for an LL AGN, NGC 3998 ($D_L = 14.1$ Mpc), to be $k_B T_e \simeq 30 - 40$ keV. However, they just observed a subtle softening in the 10–60 keV band. Our RIAF model reproduces a similar feature as shown in Fig. 1. Ref. [60] also provided the x-ray spectrum for NGC 4579 ($D_L = 16.4$ Mpc), which has a higher \dot{m} and does not show any softening feature. Our model also produces a hard power-law spectrum consistent with the observation (see Fig. 1). Thus, observing

a clear cutoff feature is necessary to determine the electron temperature, which will be achieved by future MeV satellites, such as e-ASTROGAM [58], AMEGO [61], and GRAMS [62] (see Fig. 1).

NONTHERMAL PARTICLES IN RIAFS

The protons in RIAFs can be accelerated by magnetohydrodynamic (MHD) turbulence [41, 63] and/or magnetic reconnections [64, 65] generated by the magnetorotational instability (MRI; see, e.g., Refs. [66, 67]). Here, we focus on the stochastic proton acceleration mechanism [68]. Details of the model and the cases with other acceleration mechanisms are provided in Supplemental Material and the accompanying paper [35]. We solve the diffusion equation in momentum space in which the acceleration time is written as $t_{\text{acc}} \approx \eta \beta_A^{-2} (H/c) [\varepsilon_p/(eBH)]^{2-q}$, where H is the scale height, $\beta_A = B/\sqrt{4\pi m_p n_p c^2}$ is the Alfvén velocity, η is the acceleration efficiency parameter, and q is the spectral index of the turbulence power spectrum. We consider a delta-function injection term for the stochastic acceleration process. The value of the injection energy has no influence on the resulting spectrum as long as the injection energy is much lower than the cut-off energy. The amount of nonthermal protons, or cosmic rays (CRs), is determined so that $\int L_{\varepsilon_p} d\varepsilon_p = \epsilon_p \dot{m} L_{\text{Edd}}$ is satisfied, where $L_{\varepsilon_p} = t_{\text{loss}}^{-1} \varepsilon_p dN_p/d\varepsilon_p$ is the proton luminosity [26], ϵ_p is the energy fraction carried by CRs, and $t_{\text{loss}}^{-1} = t_{\text{cool}}^{-1} + t_{\text{esc}}^{-1}$ is the total energy loss rate including cooling and escape processes. We use the Chang-Cooper method to solve the diffusion equation [69, 70]. As the proton cooling mechanism, we consider the proton synchrotron, Bethe-Heitler, photomeson, and pp inelastic collision processes. The calculation methods for the cooling timescales by these processes are given in Ref. [71]. Regarding the escape process, we only consider the infall escape. The diffusive escape is inefficient because the high-energy protons tend to move in the azimuthal direction due to the magnetic field configuration in the RIAFs [41, 63].

The CRs produce neutrinos and gamma rays through both pp and $p\gamma$ interactions. We calculate neutrino spectra from pp collisions using the formalism given by Ref. [72]. For the neutrinos by $p\gamma$ interactions, we use a semi-analytic prescription given in Refs. [26, 71, 73]. The effect of meson cooling is negligible in the RIAFs, so the neutrino flavor ratio is $\sim 1 : 1 : 1$ on Earth. The hadronic interactions also produce gamma rays and electron/positron pairs, which initiate electromagnetic cascades. We calculate the cascade emission by solving the kinetic equations of electron/positron pairs and photons (see Refs. [74, 75] for technical details). We approximately treat the pair injection processes by the Bethe-Heitler process and photomeson production as in

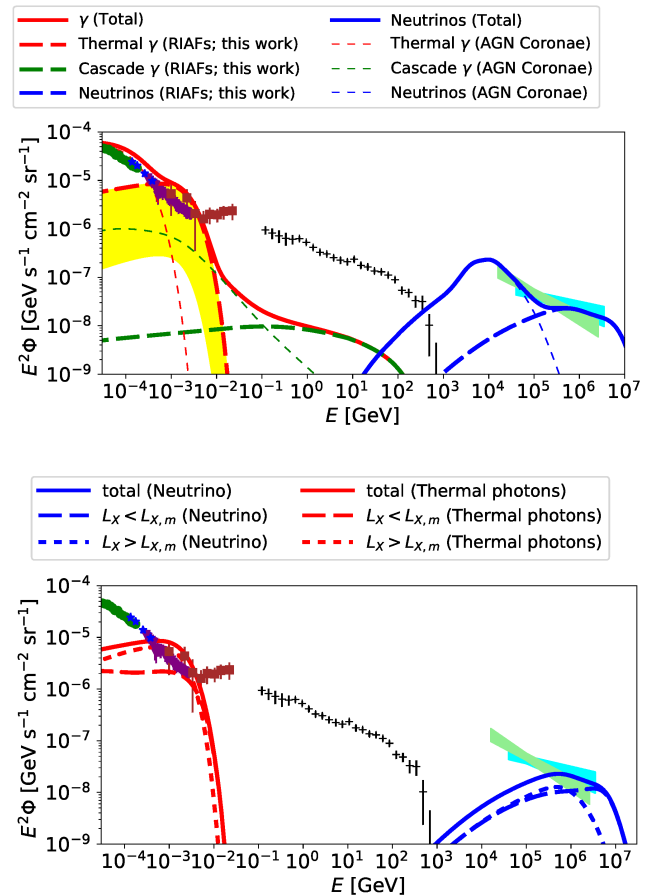


FIG. 2. Diffuse gamma-ray and all-flavor neutrino intensities. Data points are provided by *Swift-BAT* ([76]; green-circle), SMM ([77]; purple-triangle), Nagoya-balloon ([78]; blue-star), COMPTEL ([2]; red-square), *Fermi-LAT* ([3]; black-plus), and IceCube ([79, 80]; green and cyan regions). Top: Diffuse intensities for photons by thermal electrons (red), neutrinos by CR protons (blue), and gamma rays by proton-induced electromagnetic cascades (green). The thick-dashed, thin-dotted, and thick-solid lines are contributions from RIAFs in LL AGNs (this work), coronae in luminous AGNs [26], and sum of these, respectively. The yellow band in the MeV range indicates the uncertainty by the luminosity function. Bottom: Soft gamma-ray (red) and neutrino (blue) intensities from relatively luminous (dotted) and faint (dashed) LL AGNs.

Refs. [26, 35].

GAMMA-RAY AND NEUTRINO BACKGROUNDS.

We calculate the diffuse gamma-ray and neutrino intensities from the RIAFs of LL AGNs. Because the $H\alpha$ luminosity functions, $\rho_{H\alpha}$, include much fainter sources than the x-ray luminosity functions, we use $\rho_{H\alpha}$ provided by Ref. [81]: $\rho_{H\alpha} \approx \rho_*/[(L_{H\alpha}/L_*)^{s_1} + (L_{H\alpha}/L_*)^{s_2}]$,

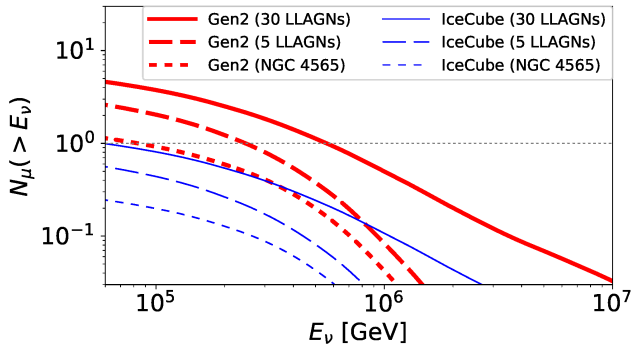


FIG. 3. The expected ν_μ -induced event number with IceCube (thin-blue) and IceCube-Gen2 (thick-red) as a function of E_ν . The solid, dashed, and dotted lines are for NGC 4565, stacking of 5 and 30 brightest LL AGNs, respectively.

where $\rho_* \approx 4.11 \times 10^{-5} \text{ Mpc}^{-3}$, $L_* = 3.26 \times 10^{41} \text{ erg s}^{-1}$, $s_1 = 2.78$, and $s_2 = 1.88$. We extrapolate this luminosity function to $L_{\min} = 10^{38} \text{ erg s}^{-1}$, below which the Palomar survey finds a hint of a break [82]. The survey also indicates a correlation between $L_{X,\text{obs}}$ and $L_{\text{H}\alpha}$ for LL AGNs: $\kappa_{X/\text{H}\alpha} = L_{X,\text{obs}}/L_{\text{H}\alpha} \simeq 6.0$ [82]. Ref. [83] provided a sample of LL AGNs, and the mean and median values of $\log(M_{\text{BH}}/\text{M}_\odot)$ are 8.0 and 8.1, respectively. Also, the x-ray luminosity density is dominated by AGNs with $M \sim 10^8 - 3 \times 10^8 \text{ M}_\odot$ if the Eddington ratio function is independent of the SMBH mass [54, 84, 85]. Thus, we set $M_{\text{BH}} = 10^8 \text{ M}_\odot$ as a reference value. Finally, we integrate the gamma-ray and neutrino fluxes over the range of $10^{38} \text{ erg s}^{-1} \leq L_{\text{H}\alpha} \leq \eta_{\text{rad,sd}} \dot{m}_{\text{crit}} L_{\text{Edd}} / (\kappa_{X/\text{H}\alpha} \kappa_{\text{bol}/X}) \simeq 4.2 \times 10^{41} \text{ erg s}^{-1}$. Since dimmer AGNs tend to have weaker redshift evolution [76, 85, 86], no redshift evolution of the luminosity function is used. We consider the gamma-ray attenuation by the extragalactic background light, and include the exponential suppression with the optical depth given in Ref. [87]. The $\gamma\gamma$ pair production initiates intergalactic electromagnetic cascades (e.g., [88]), but it has little influence on the GeV gamma-ray intensity due to the low photon cutoff energy, $E_{\gamma\gamma}$, as shown in Table I.

The top panel of Fig. 2 shows the resulting gamma-ray and neutrino intensities from LL AGNs. As shown in the bottom panel, relatively luminous LL AGNs mainly contribute to the MeV intensity. In particular, LL AGNs with $L_{\text{H}\alpha} \sim L_*$ provide the dominant contribution, which is analytically estimated to be [e.g., 89]

$$E_\gamma^2 \Phi_\gamma \sim \frac{c}{4\pi H_0} f_z \rho_* \epsilon_\gamma L_{\epsilon_\gamma} \quad (1)$$

$$\sim 9 \times 10^{-6} \text{ GeV s}^{-1} \text{ cm}^{-2} \text{ sr}^{-1} \left(\frac{f_z}{0.6} \right) \left(\frac{\epsilon_\gamma L_{\epsilon_\gamma}}{50 L_*} \right),$$

where f_z is a factor by the redshift evolution of the luminosity function [90]. This is consistent with our numeri-

cal results and the observed MeV background by COMPTEL. We stress that the resulting MeV gamma-ray intensity does not strongly depend on parameters related to the RIAF, such as α , β , M_{BH} , \dot{m}_{crit} , and the electron heating prescription, as long as we can use the luminosity function and bolometric correlation. They are dominated by the most luminous AGNs in X rays. In our RIAF model, the Comptonized emission by thermal electrons naturally accounts for the soft gamma-ray background in the 1–10 MeV range, below which canonical AGN coronae explain the x-ray background.

Furthermore, our RIAF model with a nonthermal proton component can simultaneously reproduce the IceCube data above ~ 0.3 PeV. The required pressure ratio of CRs to thermal protons is $P_{\text{CR}}/P_{\text{th}} \sim 0.01$, as shown in Table I. This value is reasonable in the sense that the CR energy density is lower than the magnetic field energy density. Interestingly, the AGN coronae above standard disks can account for medium-energy neutrinos in the 10–100 TeV range with a similar parameter set: $\eta = 10$ and $P_{\text{CR}}/P_{\text{th}} \sim 0.01$ [26]. We also plot this contribution from luminous AGNs (Seyfert galaxies and quasars) in the neutrino background. We find that our unified AGN core scenario is viable as an explanation for a wide energy range of the cosmic keV-MeV photon and TeV-PeV neutrino backgrounds, as demonstrated in Fig. 2. Note that LL AGNs with a broad range of $L_{\text{H}\alpha}$ equally contribute to the neutrino intensity for $E_\nu \sim 0.1 - 1$ PeV and the relatively fainter LL AGNs mainly emit neutrinos of $E_\nu \gtrsim 1$ PeV (see Fig. 2).

We also estimate the expected number of ν_μ -induced events from nearby LL AGNs, \mathcal{N}_μ , using the method in Refs. [71, 73] and the effective area in Ref. [91]. Stacking ~ 10 LL AGNs enables IceCube-Gen2 to detect the signal as shown in Fig. 3, although current facilities are too small to detect the signal. The atmospheric background is negligible in the energy range. The high-energy gamma rays accompanied with the neutrinos are considerably attenuated in the RIAFs, making the GeV gamma-ray intensity well below the *Fermi* data (see Fig. 2). Thus, LL AGNs are regarded as gamma-ray hidden neutrino sources [92].

SUMMARY AND DISCUSSION

We proposed RIAFs in LL AGNs as a promising guaranteed origin of the soft gamma-ray background. We constructed a one-zone model that reproduce the observed x-ray features of LL AGNs, and demonstrated that LL AGNs can also account for the high-energy neutrino background simultaneously. In the RIAFs, electrons are thermalized and emit soft gamma rays through Comptonization, suggesting a higher thermal to nonthermal transition energy than previously expected. Protons there are collisionless and naturally accelerated, produc-

ing high-energy neutrinos efficiently. Our model is consistent with the *Fermi* data in the GeV range owing to the gamma-ray attenuation inside the RIAF.

A major uncertainty for the background intensities arises from the luminosity function. Ref. [93] proposes an order of magnitude lower $\rho_{\text{H}\alpha}$ with $\rho_* = 2.0 \times 10^{-6} \text{ Mpc}^{-3}$ and $L_* = 1.0 \times 10^{42} \text{ erg s}^{-1}$. Then, an analytic estimate gives $E_\gamma^2 \Phi_\gamma \sim 1.2 \times 10^{-6} \text{ GeV s}^{-1} \text{ cm}^{-2} \text{ sr}^{-1}$, which is somewhat smaller than the observed MeV gamma-ray background. With our reference parameters, the critical H α luminosity above which RIAFs no longer exist is lower than L_* of Ref. [93], which could potentially impact on $E_\gamma^2 \Phi_\gamma$ as shown in the top panel of Fig. 2. To reproduce the IceCube neutrino data with this luminosity function, $P_{\text{CR}}/P_{\text{th}} \gtrsim 0.3$ is necessary. Even with such a strong CR pressure, the dynamical structure of the RIAFs does not change [94] as long as CRs are confined in the flow. In this situation, the gamma rays from proton-induced cascades are enhanced, and we expect the detection of high-energy gamma-ray by *Fermi* LAT from nearby LL AGNs. However, such a high CR pressure is at odds with the assumption that the turbulence energy is the source of the CRs. The uncertainty in the luminosity function should be palliated by future surveys using a line-sensitive optical instrument or a sensitive x-ray satellite, such as PFS [95] or eROSITA [96] and FORCE [97].

High-energy multimessenger observations are essential to identify the origin of the gamma-ray and neutrino backgrounds. Point-source detections of nearby LL AGNs are challenging for the present IceCube but hard x rays detected from several sources are consistent with our RIAF model. Planned experiments, such as IceCube-Gen2 [98] and the proposed MeV satellites, will be able to detect the neutrino signals and thermal MeV gamma rays including the cutoff feature from the nearby LL AGNs. Our model will be concretely tested by future multimessenger observations as discussed in the accompanying paper [35]. Especially, future MeV gamma-ray observations may determine the electron temperature in RIAFs, which will shed light on electron heating mechanisms in magnetized collisionless plasmas. The electron temperature in RIAFs also affects the interpretation of the photon ring observed by the Event Horizon Telescope [99, 100]. The emission region of the observed photon ring is determined by the electron temperature and magnetization, which should be clarified by a future multi-wavelength modeling of nearby LL AGNs. Furthermore, the anisotropy tests for MeV gamma rays are promising [101], and our RIAF model predicts a smaller anisotropy than those of Seyfert and FSRQ models.

This work is supported in part by the IGC postdoctoral fellowship program, JSPS Oversea Research Fellowship, JSPS Research Fellowship, KAKENHI Nos. 19J00198 (S.S.K.), the Alfred P. Sloan Foundation, NSF Grant No. AST-1908689, and KAKENHI No. 20H01901 (K.M.),

and the Eberly Foundation (P.M.).

- [1] A. C. Fabian and X. Barcons, Annual Review of Astronomy and Astrophysics **30**, 429 (1992).
- [2] G. Weidenspointner, M. Varendorff, S. C. Kappadath, K. Bennett, H. Bloemen, R. Diehl, W. Hermsen, G. G. Lichti, J. Ryan, and V. Schönfelder, in *American Institute of Physics Conference Series*, Vol. 510, edited by M. L. McConnell and J. M. Ryan (2000) pp. 467–470.
- [3] M. Ackermann *et al.* (Fermi-LAT), *Astrophys. J.* **799**, 86 (2015), arXiv:1410.3696 [astro-ph.HE].
- [4] M. G. Aartsen, R. Abbasi, Y. Abdou, M. Ackermann, J. Adams, J. A. Aguilar, M. Ahlers, D. Altmann, J. Auffenberg, X. Bai, and et al., *Physical Review Letters* **111**, 021103 (2013), arXiv:1304.5356 [astro-ph.HE].
- [5] IceCube Collaboration, *Science* **342**, 1242856 (2013), arXiv:1311.5238 [astro-ph.HE].
- [6] M. G. Aartsen, K. Abraham, M. Ackermann, J. Adams, J. A. Aguilar, M. Ahlers, M. Ahrens, D. Altmann, T. Anderson, M. Archinger, and et al., *ApJ* **809**, 98 (2015), arXiv:1507.03991 [astro-ph.HE].
- [7] M. G. Aartsen, M. Ackermann, J. Adams, J. A. Aguilar, M. Ahlers, M. Ahrens, D. Altmann, T. Anderson, C. Arguelles, T. C. Arlen, and et al., *Physical Review Letters* **113**, 101101 (2014), arXiv:1405.5303 [astro-ph.HE].
- [8] M. G. Aartsen *et al.* (IceCube), *Phys. Rev. Lett.* **115**, 081102 (2015), arXiv:1507.04005 [astro-ph.HE].
- [9] Y. Ueda, M. Akiyama, K. Ohta, and T. Miyaji, *ApJ* **598**, 886 (2003), astro-ph/0308140.
- [10] M. Fornasa and M. A. Sánchez-Conde, *Phys. Rep.* **598**, 1 (2015), arXiv:1502.02866 [astro-ph.CO].
- [11] Y. Inoue, arXiv e-prints , arXiv:1412.3886 (2014), arXiv:1412.3886 [astro-ph.HE].
- [12] D. D. Clayton and R. A. Ward, *ApJ* **198**, 241 (1975).
- [13] K. Watanabe, D. H. Hartmann, M. D. Leising, and L. S. The, *ApJ* **516**, 285 (1999), arXiv:astro-ph/9809197 [astro-ph].
- [14] A. W. Strong, A. W. Wolfendale, and D. M. Worrall, *Journal of Physics A Mathematical General* **9**, 1553 (1976).
- [15] M. Ajello, L. Costamante, R. M. Sambruna, N. Gehrels, J. Chiang, A. Rau, A. Escala, J. Greiner, J. Tueller, J. V. Wall, and R. F. Mushotzky, *ApJ* **699**, 603 (2009), arXiv:0905.0472 [astro-ph.CO].
- [16] K. A. Olive and J. Silk, *Phys. Rev. Lett.* **55**, 2362 (1985).
- [17] K. Ahn and E. Komatsu, *Phys. Rev. D* **72**, 061301 (2005), arXiv:astro-ph/0506520 [astro-ph].
- [18] J. F. Beacom, N. F. Bell, and G. Bertone, *Phys. Rev. Lett.* **94**, 171301 (2005), arXiv:astro-ph/0409403 [astro-ph].
- [19] L. E. Strigari, J. F. Beacom, T. P. Walker, and P. Zhang, *J. Cosmology Astropart. Phys.* **2005**, 017 (2005),

arXiv:astro-ph/0502150 [astro-ph].

[20] Y. Inoue, ApJ **733**, 66 (2011), arXiv:1103.3946 [astro-ph.HE].

[21] P. Ruiz-Lapuente, L.-S. The, D. H. Hartmann, M. Ajello, R. Canal, F. K. Röpke, S. T. Ohlmann, and W. Hillebrandt, ApJ **820**, 142 (2016), arXiv:1502.06116 [astro-ph.HE].

[22] M. Ajello, M. S. Shaw, R. W. Romani, C. D. Dermer, L. Costamante, O. G. King, W. Max-Moerbeck, A. Readhead, A. Reimer, J. L. Richards, and M. Stevenson, ApJ **751**, 108 (2012), arXiv:1110.3787 [astro-ph.CO].

[23] F. W. Stecker, M. H. Salamon, and C. Done, arXiv e-prints , astro-ph/9912106 (1999), arXiv:astro-ph/9912106 [astro-ph].

[24] Y. Inoue, T. Totani, and Y. Ueda, ApJ **672**, L5 (2008), arXiv:0709.3877 [astro-ph].

[25] Y. Inoue, D. Khangulyan, S. Inoue, and A. Doi, ApJ **880**, 40 (2019), arXiv:1904.00554 [astro-ph.HE].

[26] K. Murase, S. S. Kimura, and P. Meszaros, arXiv e-prints , arXiv:1904.04226 (2019), arXiv:1904.04226 [astro-ph.HE].

[27] R. Narayan and I. Yi, ApJ **428**, L13 (1994), astro-ph/9403052.

[28] R. D. Blandford and M. C. Begelman, MNRAS **303**, L1 (1999), astro-ph/9809083.

[29] F. Yuan and R. Narayan, ARA&A **52**, 529 (2014), arXiv:1401.0586 [astro-ph.HE].

[30] S. S. Kimura, K. Murase, and K. Toma, ApJ **806**, 159 (2015), arXiv:1411.3588 [astro-ph.HE].

[31] B. Khiali and E. M. de Gouveia Dal Pino, MNRAS **455**, 838 (2016), arXiv:1506.01063 [astro-ph.HE].

[32] K. Hayasaki and R. Yamazaki, ApJ **886**, 114 (2019).

[33] J. C. Rodríguez-Ramírez, E. M. de Gouveia Dal Pino, and R. Alves Batista, ApJ **879**, 6 (2019), arXiv:1904.05765 [astro-ph.HE].

[34] S. S. Kimura and K. Toma, arXiv e-prints , arXiv:2003.13173 (2020), arXiv:2003.13173 [astro-ph.HE].

[35] S. S. Kimura, K. Murase, and P. Mészáros, Phys. Rev. D **100**, 083014 (2019), arXiv:1908.08421 [astro-ph.HE].

[36] K. Ohsuga and S. Mineshige, ApJ **736**, 2 (2011), arXiv:1105.5474 [astro-ph.HE].

[37] R. Narayan, A. Sädowski, R. F. Penna, and A. K. Kulkarni, MNRAS **426**, 3241 (2012), arXiv:1206.1213 [astro-ph.HE].

[38] R. F. Penna, A. Sädowski, A. K. Kulkarni, and R. Narayan, MNRAS **428**, 2255 (2013), arXiv:1211.0526 [astro-ph.HE].

[39] S. M. Ressler, A. Tchekhovskoy, E. Quataert, and C. F. Gammie, MNRAS **467**, 3604 (2017), arXiv:1611.09365 [astro-ph.HE].

[40] A. Chael, M. Rowan, R. Narayan, M. Johnson, and L. Sironi, MNRAS **478**, 5209 (2018), arXiv:1804.06416 [astro-ph.HE].

[41] S. S. Kimura, K. Tomida, and K. Murase, MNRAS **485**, 163 (2019), arXiv:1812.03901 [astro-ph.HE].

[42] N. I. Shakura and R. A. Sunyaev, A&A **24**, 337 (1973).

[43] R. G. Martin, C. J. Nixon, J. E. Pringle, and M. Livio, New A **70**, 7 (2019).

[44] A. Chael, R. Narayan, and M. D. Johnson, MNRAS **486**, 2873 (2019), arXiv:1810.01983 [astro-ph.HE].

[45] J. E. Pringle, ARA&A **19**, 137 (1981).

[46] R. Narayan and I. Yi, ApJ **452**, 710 (1995), astro-ph/9411059.

[47] R. Mahadevan and E. Quataert, ApJ **490**, 605 (1997), astro-ph/9705067.

[48] R. Mahadevan, ApJ **477**, 585 (1997), astro-ph/9609107.

[49] F.-G. Xie and F. Yuan, MNRAS **427**, 1580 (2012), arXiv:1207.3113 [astro-ph.HE].

[50] L. Sironi and R. Narayan, ApJ **800**, 88 (2015), arXiv:1411.5685 [astro-ph.HE].

[51] L. Sironi, ApJ **800**, 89 (2015), arXiv:1411.6014 [astro-ph.HE].

[52] V. Zhdankin, D. A. Uzdensky, G. R. Werner, and M. C. Begelman, Phys. Rev. Lett. **122**, 055101 (2019), arXiv:1809.01966 [astro-ph.HE].

[53] Y. Kawazura, M. Barnes, and A. A. Schekochihin, Proceedings of the National Academy of Science **116**, 771 (2019), arXiv:1807.07702 [physics.plasm-ph].

[54] A. Marconi, G. Risaliti, R. Gilli, L. K. Hunt, R. Maiolino, and M. Salvati, MNRAS **351**, 169 (2004), astro-ph/0311619.

[55] P. F. Hopkins, G. T. Richards, and L. Hernquist, ApJ **654**, 731 (2007), arXiv:astro-ph/0605678 [astro-ph].

[56] E. Lusso, A. Comastri, B. D. Simmons, M. Mignoli, G. Zamorani, C. Vignali, M. Brusa, F. Shankar, D. Lutz, J. R. Trump, R. Maiolino, R. Gilli, M. Bolzonella, S. Puccetti, M. Salvato, C. D. Impey, F. Civano, M. Elvis, V. Mainieri, J. D. Silverman, A. M. Koekemoer, A. Bongiorno, A. Merloni, S. Berta, E. Le Floc'h, B. Magnelli, F. Pozzi, and L. Riguccini, MNRAS **425**, 623 (2012), arXiv:1206.2642 [astro-ph.CO].

[57] Z. Liu, A. Merloni, A. Georgakakis, M.-L. Menzel, J. Buchner, K. Nandra, M. Salvato, Y. Shen, M. Brusa, and A. Streblyanska, MNRAS **459**, 1602 (2016), arXiv:1605.00207 [astro-ph.HE].

[58] A. De Angelis, V. Tatischeff, M. Tavani, U. Oberlack, I. Grenier, L. Hanlon, R. Walter, A. Argan, P. von Ballmoos, and A. Bulgarelli, Experimental Astronomy **44**, 25 (2017), arXiv:1611.02232 [astro-ph.HE].

[59] G. B. Rybicki and A. P. Lightman, *New York, Wiley-Interscience, 1979.* 393 p. (1979).

[60] G. Younes, A. Ptak, L. C. Ho, F.-G. Xie, Y. Terasima, F. Yuan, D. Huppenkothen, and M. Yukita, ApJ **870**, 73 (2019), arXiv:1811.10657 [astro-ph.GA].

[61] A. Moiseev and Amego Team, International Cosmic Ray Conference **301**, 798 (2017).

[62] T. Aramaki, P. O. H. Adrian, G. Karagiorgi, and H. Odaka, Astroparticle Physics **114**, 107 (2020), arXiv:1901.03430 [astro-ph.HE].

[63] S. S. Kimura, K. Toma, T. K. Suzuki, and S.-i. Inutsuka, ApJ **822**, 88 (2016), arXiv:1602.07773 [astro-ph.HE].

[64] M. Hoshino, Physical Review Letters **114**, 061101 (2015), arXiv:1502.02452 [astro-ph.HE].

[65] M. W. Kunz, J. M. Stone, and E. Quataert, Physical Review Letters **117**, 235101 (2016), arXiv:1608.07911 [astro-ph.HE].

[66] S. A. Balbus and J. F. Hawley, *ApJ* **376**, 214 (1991).

[67] S. A. Balbus and J. F. Hawley, *Reviews of Modern Physics* **70**, 1 (1998).

[68] V. Petrosian, *Space Sci. Rev.* **173**, 535 (2012), arXiv:1205.2136 [astro-ph.HE].

[69] J. S. Chang and G. Cooper, *Journal of Computational Physics* **6**, 1 (1970).

[70] B. T. Park and V. Petrosian, *The Astrophysical Journal Supplement Series* **103**, 255 (1996).

[71] S. S. Kimura, K. Murase, I. Bartos, K. Ioka, I. S. Heng, and P. Mészáros, *Phys. Rev. D* **98**, 043020 (2018), arXiv:1805.11613 [astro-ph.HE].

[72] S. R. Kelner, F. A. Aharonian, and V. V. Bugayov, *Phys. Rev. D* **74**, 034018 (2006), astro-ph/0606058.

[73] S. S. Kimura, K. Murase, P. Mészáros, and K. Kiuchi, *ApJ* **848**, L4 (2017), arXiv:1708.07075 [astro-ph.HE].

[74] K. Murase, *Phys. Rev. D* **97**, 081301 (2018), arXiv:1705.04750 [astro-ph.HE].

[75] K. Murase, A. Franckowiak, K. Maeda, R. Margutti, and J. F. Beacom, *ApJ* **874**, 80 (2019), arXiv:1807.01460 [astro-ph.HE].

[76] M. Ajello, R. W. Romani, D. Gasparrini, M. S. Shaw, J. Bolmer, G. Cotter, J. Finke, J. Greiner, S. E. Healey, O. King, W. Max-Moerbeck, P. F. Michelson, W. J. Potter, A. Rau, A. C. S. Readhead, J. L. Richards, and P. Schady, *ApJ* **780**, 73 (2014), arXiv:1310.0006 [astro-ph.CO].

[77] K. Watanabe, D. H. Hartmann, M. D. Leising, L. S. The, G. H. Share, and R. L. Kinzer, in *Proceedings of the Fourth Compton Symposium*, American Institute of Physics Conference Series, Vol. 410, edited by C. D. Dermer, M. S. Strickman, and J. D. Kurfess (1997) pp. 1223–1227.

[78] Y. Fukada, S. Hayakawa, I. Kasahara, F. Makino, Y. Tanaka, and B. V. Sreekantan, *Nature* **254**, 398 (1975).

[79] M. G. Aartsen *et al.* (IceCube), (2020), arXiv:2001.09520 [astro-ph.HE].

[80] J. Stettner, in *36th International Cosmic Ray Conference (ICRC2019)*, International Cosmic Ray Conference, Vol. 36 (2019) p. 1017, arXiv:1908.09551 [astro-ph.HE].

[81] L. Hao, M. A. Strauss, X. Fan, C. A. Tremonti, D. J. Schlegel, T. M. Heckman, G. Kauffmann, M. R. Blanton, J. E. Gunn, P. B. Hall, Ž. Ivezić, G. R. Knapp, J. H. Krolík, R. H. Lupton, G. T. Richards, D. P. Schneider, I. V. Strateva, N. L. Zakamska, J. Brinkmann, and G. P. Szokoly, *AJ* **129**, 1795 (2005), astro-ph/0501042.

[82] L. C. Ho, *ARA&A* **46**, 475 (2008), arXiv:0803.2268.

[83] P. Saikia, E. Körding, D. L. Coppejans, H. Falcke, D. Williams, R. D. Baldi, I. Mchardy, and R. Beswick, *A&A* **616**, A152 (2018), arXiv:1805.06696 [astro-ph.HE].

[84] Y.-R. Li, L. C. Ho, and J.-M. Wang, *ApJ* **742**, 33 (2011), arXiv:1109.0089 [astro-ph.CO].

[85] Y. Ueda, M. Akiyama, G. Hasinger, T. Miyaji, and M. G. Watson, *ApJ* **786**, 104 (2014), arXiv:1402.1836 [astro-ph.CO].

[86] P. Padovani, N. Miller, K. I. Kellermann, V. Mainieri, P. Rosati, and P. Tozzi, *ApJ* **740**, 20 (2011), arXiv:1107.2759.

[87] A. Franceschini and G. Rodighiero, *A&A* **603**, A34 (2017), arXiv:1705.10256 [astro-ph.HE].

[88] K. Murase, J. F. Beacom, and H. Takami, *Journal of Cosmology and Astro-Particle Physics* **2012**, 030 (2012), arXiv:1205.5755 [astro-ph.HE].

[89] K. Murase, Y. Inoue, and C. D. Dermer, *Phys. Rev. D* **90**, 023007 (2014), arXiv:1403.4089 [astro-ph.HE].

[90] K. Murase and E. Waxman, *Phys. Rev. D* **94**, 103006 (2016), arXiv:1607.01601 [astro-ph.HE].

[91] M. G. Aartsen, K. Abraham, M. Ackermann, J. Adams, J. A. Aguilar, M. Ahlers, M. Ahrens, D. Altmann, K. Andeen, T. Anderson, and et al., *ApJ* **835**, 151 (2017), arXiv:1609.04981 [astro-ph.HE].

[92] K. Murase, D. Guetta, and M. Ahlers, *Phys. Rev. Lett.* **116**, 071101 (2016), arXiv:1509.00805 [astro-ph.HE].

[93] J. E. Greene and L. C. Ho, *ApJ* **667**, 131 (2007), arXiv:0705.0020 [astro-ph].

[94] S. S. Kimura, K. Toma, and F. Takahara, *ApJ* **791**, 100 (2014), arXiv:1407.0115 [astro-ph.HE].

[95] M. Takada, R. S. Ellis, M. Chiba, J. E. Greene, H. Aihara, N. Arimoto, K. Bundy, J. Cohen, O. Doré, and G. Graves, *PASJ* **66**, R1 (2014), arXiv:1206.0737 [astro-ph.CO].

[96] A. Merloni, P. Predehl, W. Becker, H. Böhringer, T. Boller, H. Brunner, M. Brusa, K. Dennerl, M. Freyberg, P. Friedrich, A. Georgakakis, F. Haberl, G. Hasinger, N. Meidinger, J. Mohr, K. Nandra, A. Rau, T. H. Reiprich, J. Robrade, M. Salvato, A. Santangelo, M. Sasaki, A. Schwope, J. Wilms, and t. German eROSITA Consortium, ArXiv e-prints (2012), arXiv:1209.3114 [astro-ph.HE].

[97] K. Mori, T. G. Tsuru, K. Nakazawa, Y. Ueda, T. Okajima, H. Murakami, H. Awaki, H. Matsumoto, Y. Fukazawa, H. Tsunemi, T. Takahashi, and W. W. Zhang, “A broadband x-ray imaging spectroscopy with high-angular resolution: the FORCE mission,” in *Proc. SPIE, Society of Photo-Optical Instrumentation Engineers (SPIE) Conference Series*, Vol. 9905 (2016) p. 99051O.

[98] M. G. Aartsen *et al.* (IceCube), (2014), arXiv:1412.5106 [astro-ph.HE].

[99] K. Akiyama *et al.* (Event Horizon Telescope), *Astrophys. J.* **875**, L1 (2019), arXiv:1906.11238 [astro-ph.GA].

[100] K. Akiyama *et al.* (Event Horizon Telescope), *Astrophys. J.* **875**, L5 (2019), arXiv:1906.11242 [astro-ph.GA].

[101] Y. Inoue, K. Murase, G. M. Madejski, and Y. Uchiyama, *ApJ* **776**, 33 (2013), arXiv:1308.1951 [astro-ph.CO].

Supplemental Material

Soft photon spectra with various parameters

We calculate the soft photon spectra using the method given in Refs. [30, 35]. To see the parameter dependence, we plot the soft photon spectra for various values of $L_{X,\text{obs}}$ and β in Fig. S1. For the cases with $m \gtrsim 3 \times 10^{-3}$, i.e., the cases with $\log L_{X,\text{obs}} \gtrsim 40.6$, the Comptonization process dominates over the other cooling processes, making a bump in the MeV band. Lower values of β make the synchrotron emission more efficient, leading to lower values of the electron temperature. The Comptonization in such cases is weaker, and thus, the MeV bump is blunt, compared to the cases with a high value of β .

Stochastic proton acceleration in RIAFs

Here, we describe the details of the stochastic acceleration model. To obtain the CR spectrum, we solve the diffusion equation in the momentum space:

$$\frac{\partial \mathcal{F}_p}{\partial t} = \frac{1}{\varepsilon_p^2} \frac{\partial}{\partial \varepsilon_p} \left(\varepsilon_p^2 D_{\varepsilon_p} \frac{\partial \mathcal{F}_p}{\partial \varepsilon_p} + \frac{\varepsilon_p^3}{t_{\text{cool}}} \mathcal{F}_p \right) - \frac{\mathcal{F}_p}{t_{\text{esc}}} + \dot{\mathcal{F}}_{p,\text{inj}}, \quad (\text{S1})$$

where \mathcal{F}_p is the momentum distribution function for protons ($dN/d\varepsilon_p = 4\pi p^2 \mathcal{F}_p/c$), D_{ε_p} is the diffusion coefficient, t_{cool} is the cooling time for protons, t_{esc} is the escape time, and $\dot{\mathcal{F}}_{p,\text{inj}}$ is the injection function. Assuming the gyro-resonant scattering, we can write

$$D_{\varepsilon_p} \approx \frac{c \beta_A^2}{\eta H} \left(\frac{r_L}{H} \right)^{q-2} \varepsilon_p^2, \quad (\text{S2})$$

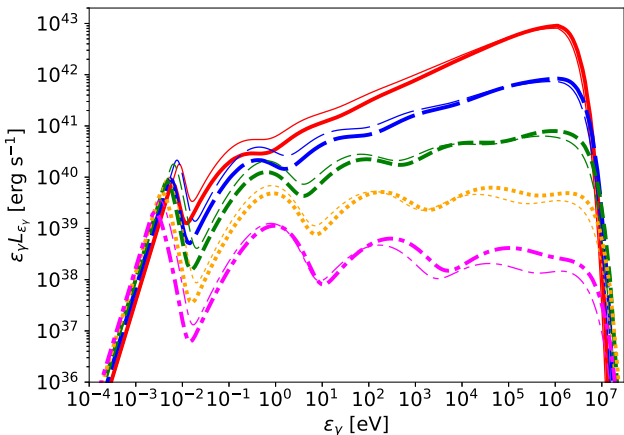


FIG. S1. Photon spectrum from thermal electrons in RIAFs with various $L_{X,\text{obs}}$. The thick and thin lines are for the cases with $\beta = 10$ and $\beta = 3$, respectively. The values of $\log L_{X,\text{obs}}$ are 38.78, 39.68, 40.59, 41.50, and 42.40 from bottom to top.

where $r_L = \varepsilon_p/(eB)$ is the Larmor radius, $\eta = B^2/(8\pi \int P_k dk)$ is the turbulence parameter (P_k is the turbulence power spectrum), and q is the power-law index of P_k . The details of the calculation methods for the cooling and escape times are written in the accompanying paper [35] (see also Refs. [26, 30]).

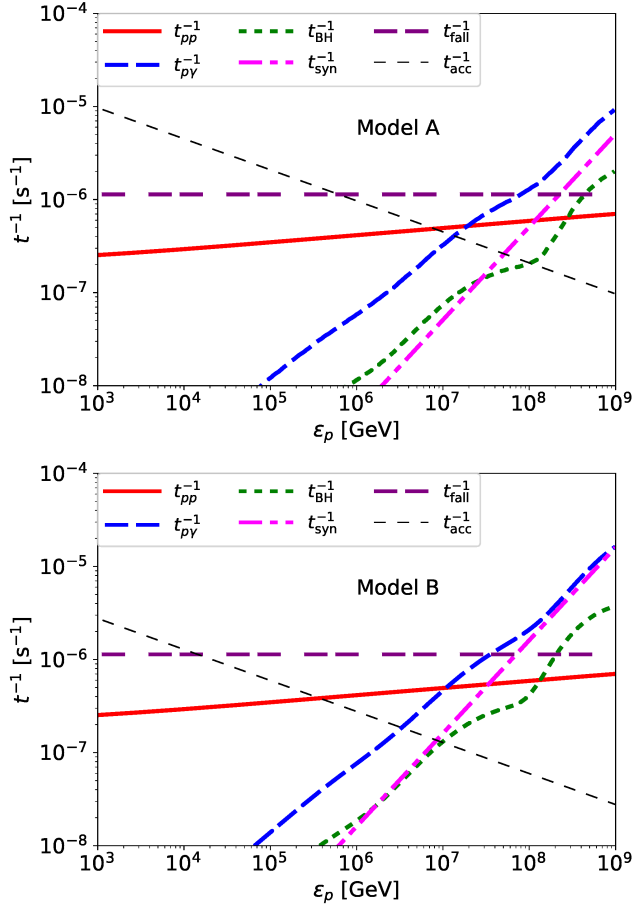
In Fig. S2, we plot the acceleration and loss rates of CRs for model A (top; shown in the main text) and B (bottom; accounting for TeV-PeV neutrinos) for the case with $\log L_{X,\text{obs}} = 41.50$ ($m \simeq 10^{-2}$) and parameter sets in Table S1. We estimate timescales of pp inelastic collisions (t_{pp}), photomeson production ($t_{p\gamma}$), Bethe-Heitler pair production (t_{BH}), proton synchrotron (t_{syn}), infall escape (t_{fall}), and acceleration (t_{acc}). For both models, the dominant loss process is the infall escape for the range of our interest. The infall escape and pp collision do not produce a strong cutoff due to their weak energy dependence. On the other hand, photomeson production leads to a sharp cutoff, which determines the peak energy of the resulting proton spectrum (see Fig. S3). Neutrinos are mainly produced by the pp collisions for $\varepsilon_p \lesssim 10^7$ GeV, and the photomeson production is effective above the energy. Bethe-Heitler and proton synchrotron processes are always subdominant in our RIAF model. For higher $L_{X,\text{obs}}$ cases, the photomeson production is more efficient, and hence, the peak energy of the proton spectrum is lower.

Fig. S3 shows the resulting spectra of protons, per-flavor neutrinos, and gamma rays by proton-induced electromagnetic cascades for $\log L_{X,\text{obs}} = 41.50$ for models A (top) and B (bottom). The proton spectrum has a peak around 10 PeV (1 PeV) for model A (B), and hard power-law spectra are achieved below the peak. For model A, neutrinos are predominantly produced by pp interaction for $\varepsilon_p \lesssim 1$ PeV, while $p\gamma$ interactions provide a dominant contribution above the energy. For model B, neutrinos are mainly produced by pp interactions, although $p\gamma$ interactions give a comparable contribution around the peak energy. For both models, the cascade gamma-ray spectra have a flat spectra below the $\gamma\gamma$ pair-production cutoff energy, $E_{\gamma\gamma}$ (see Table I), as often seen in well-developed cascades. The cascade gamma-ray luminosity is comparable to the neutrino luminosity.

The upper panel of Fig. S4 depicts the diffuse gamma-ray and neutrino intensities for models A and B. Model B has a lower β , which strengthens the synchrotron emission. This leads to a slightly weaker Comptonization bump in the MeV range. Hence, the soft gamma-ray intensity is lower than that for model A, although the effect is subtle. The neutrino intensity is normalized such that it matches the observed TeV-PeV neutrinos. This is about an order of magnitude higher than that for model A, but the resulting gamma-ray intensity by proton-induced cascades is still considerably lower than the Fermi data. Therefore, our LL AGN model can be the source of mysterious TeV-PeV neutrinos.

Parameters	β	$\epsilon_p/10^{-3}$	η	s_{inj}	$\eta_{\text{acc}}/10^5$
Model A	10	0.30	10	-	-
Model B	3.2	3.0	133	-	-
Model C	10	0.30	-	1.0	0.30
Model D	3.2	2.0	-	1.0	10
Model E	10	2.0	-	2.0	0.10
Model F	3.2	10	-	2.0	2.0

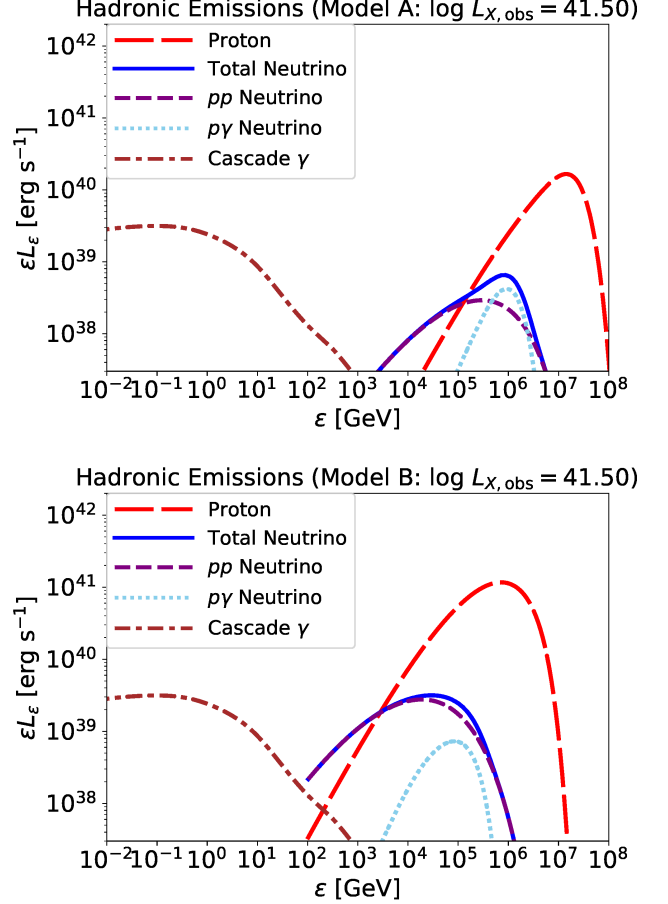
TABLE S1. Parameters for stochastic acceleration models.

FIG. S2. Acceleration and loss rates as a function of the proton energy for model A (top) and B (bottom) with $\log L_{X,\text{obs}} = 40.50$.

Power-law injection models for CRs

If protons are accelerated by another mechanism, such as magnetic reconnection, the CR spectrum can be obtained by solving the transport equation with a power-law injection term:

$$\frac{d}{d\epsilon_p} \left(-\frac{\epsilon_p}{t_{\text{cool}}} N_{\epsilon_p} \right) = \dot{N}_{\epsilon_p,\text{inj}} - \frac{N_{\epsilon_p}}{t_{\text{esc}}}, \quad (\text{S3})$$

FIG. S3. Spectra for protons (long-dashed), photons by proton-induced electromagnetic cascades (dot-dashed), per-flavor neutrinos by pp (short-dashed), $p\gamma$ (dotted), and sum of them (solid). The top and bottom panels are for model A and B, respectively.

$$\dot{N}_{\epsilon_p,\text{inj}} = \dot{N}_0 \left(\frac{\epsilon_p}{\epsilon_{p,\text{cut}}} \right)^{-s_{\text{inj}}} \exp \left(-\frac{\epsilon_p}{\epsilon_{p,\text{cut}}} \right), \quad (\text{S4})$$

where $\epsilon_{p,\text{cut}}$ is the cutoff energy for the injected protons and \dot{N}_0 is the normalization factor. The injection is normalized such that $\int \epsilon_p \dot{N}_{\epsilon_p,\text{inj}} d\epsilon_p = \epsilon_p \dot{m} L_{\text{Edd}}$ is satisfied. We estimate $\epsilon_{p,\text{max}}$ by equating the infall timescale to the acceleration timescale, t_{acc} . We set $t_{\text{acc}} = \eta_{\text{acc}} r L/c$, where η_{acc} is the acceleration efficiency parameter. Equation (S3) has an analytic solution:

$$N_{\epsilon_p} = \frac{t_{\text{cool}}}{\epsilon_p} \int_{\epsilon_p}^{\infty} d\epsilon'_p \dot{N}_{\epsilon_p,\text{inj}}(\epsilon'_p) \exp(-\mathcal{G}(\epsilon_p, \epsilon'_p)), \quad (\text{S5})$$

$$\mathcal{G}(\epsilon_1, \epsilon_2) = \int_{\epsilon_1}^{\epsilon_2} \frac{t_{\text{cool}}}{t_{\text{esc}}} \frac{d\epsilon'_p}{\epsilon'_p}. \quad (\text{S6})$$

The cooling and loss processes are the same with the stochastic acceleration model. See the accompanying paper [35] for details.

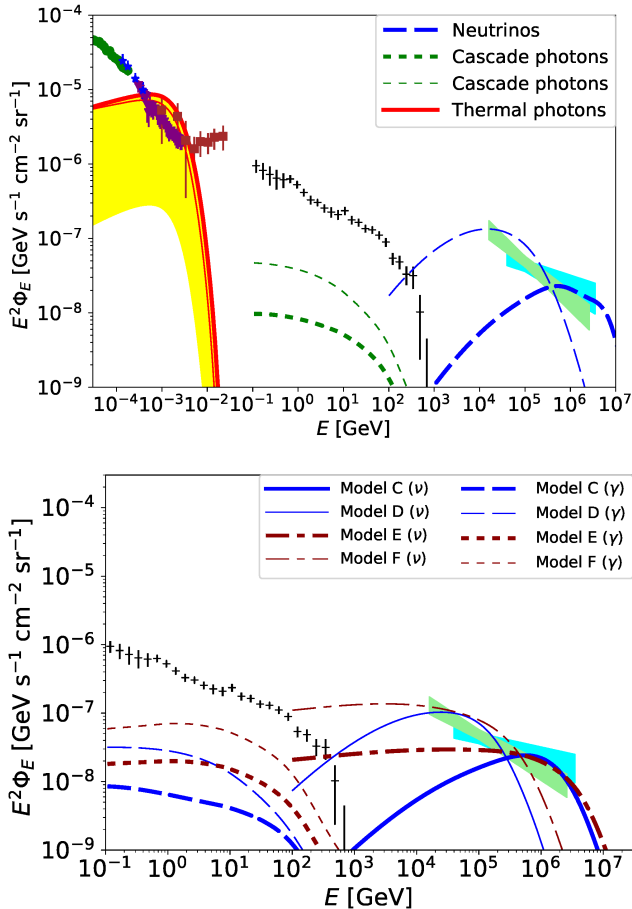


FIG. S4. Diffuse all-flavor neutrino and gamma-ray intensities. Data points are the same with Fig. 2. Top: Models for the stochastic acceleration cases. The thick and thin lines are for models A and B, respectively. The red-solid, blue-dashed, and green-dotted lines are for gamma rays by thermal electrons, neutrinos by hadronic interactions, and gamma rays by proton-induced electromagnetic cascades, respectively. Bottom: Models for power-law injection cases. The thick-solid, thin-solid, thick-dotted-dashed, and thin-dotted-dashed lines are high-energy neutrino intensities for models C, D, E, and F, respectively. The thick-dashed, thin-dashed, thick-dotted, and thin-dotted lines are gamma-ray intensities by proton-induced electromagnetic cascades for models C, D, E, and F, respectively.

In Fig. S4, we plot the diffuse neutrino and gamma-ray intensities for the power-law injection models with the parameter sets tabulated in Table S1. Models C and E explain PeV neutrinos, while models D and F reproduce 10–100 TeV neutrinos. The cascade gamma-ray emissions are well below the Fermi data owing to the low $\gamma\gamma$ cutoff energy in the RIAFs. Note that the resulting diffuse MeV gamma-ray intensities for models C and E (D and F) are the same as that for model A (B), because the thermal electrons in the RIAFs are

identical. The CR pressure required to achieve the observed neutrino intensity is $P_{\text{CR}}/P_{\text{th}} \sim 0.01$ for model C, $P_{\text{CR}}/P_{\text{th}} \sim 0.1$ for model D, $P_{\text{CR}}/P_{\text{th}} \sim 0.1$ for model E, and $P_{\text{CR}}/P_{\text{th}} \sim 0.5$ for model F. A higher $P_{\text{CR}}/P_{\text{th}}$ is demanded for a higher s_{inj} and for 10–100 TeV neutrinos. In the accompanying paper, we estimate the point-source detectability of the neutrinos from nearby LL AGNs with the parameter sets for models B, D, and F, and show that the TeV–PeV neutrinos and MeV gamma-rays are detectable with the planned neutrino and gamma-ray experiments, IceCube-Gen2 and AMEGO/eASTROGAM/GRAMS, respectively.

Remarks on previous works

The present work is different from the previous works. Ref. [30] calculated the neutrino background from RIAFs, considering stochastic particle acceleration by MHD turbulence. It indicated that the RIAFs can account for the neutrino background for either 10–100 TeV or for 0.1–1 PeV, but did not estimate the gamma-ray emission and neutrino point-source detectability. Recently, Ref. [35] estimated the neutrino and gamma-ray emissions from RIAFs in nearby LL AGNs using a similar model, and discuss the neutrino and gamma-ray detectabilities from nearby LL AGNs. In addition to the stochastic acceleration model, the power-law injection models were discussed. The electromagnetic cascades initiated by the hadronic processes were also taken into account. Ref. [34] considered the gamma-ray and neutrino emissions from magnetically arrested disks (MADs) in radio galaxies. The efficient acceleration that is nearly the theoretical limit is assumed. This could be possible by magnetic reconnections, and the maximum energy of the accelerated particles is much higher than the other papers. However, it ignored acceleration of primary electrons and did not calculate electromagnetic cascades, but the gamma-ray attenuation by the two-photon annihilation process was taken into account.

In the present work, we focused on the high-energy background radiation from LL AGNs, and acceleration in the bulk of accretion disks are considered. On the other hand, Ref. [26] calculated the neutrino and gamma-ray emissions from hot coronae surrounding the accretion disk in Seyfert galaxies and quasars, fully taking into account electromagnetic cascades. It showed that Seyfert galaxies and quasars can account for the X-ray and 10–100 TeV neutrino backgrounds that require gamma-ray hidden sources. Although these objects and LL AGNs belong to different populations of AGNs, for the first time we showed that the unified AGN core model can simultaneously explain the X-ray and MeV gamma-ray backgrounds without nonthermal electrons, together with the TeV–PeV neutrino background with relativistic protons. Strictly speaking, the prescription of the nonthermal par-

ticle injection for our RIAF model is also different from that for the AGN corona model in Ref. [26]. In the RIAF model, we use a constant ϵ_p parameter, i.e., the fraction of CR luminosity to the accretion luminosity is independent of \dot{m} . On the other hand, in the AGN corona model, we considered that $\dot{\mathcal{F}}_{p,\text{inj}}$ is proportional to L_X . In the latter treatment, ϵ_p depends on L_X and \dot{m} . The injection process of nonthermal CR acceleration remains an open problem, so we examined effects of both pre-

scriptions. We find that our RIAF model can reproduce 0.1–1 PeV neutrino data with either of the prescriptions, with a similar value of $P_{\text{CR}}/P_{\text{th}} \sim 0.01$. The results for higher-luminosity LL AGNs are almost identical for our RIAF model, and our conclusions are nearly independent of these prescriptions about the injection. Also, the AGN corona model with a constant ϵ_p parameter can reproduce the IceCube neutrino data of 10–100 TeV with a similar $P_{\text{CR}}/P_{\text{th}}$, because the AGNs with $L_X \sim 10^{44}$ erg s^{−1} predominantly contribute to the diffuse intensities.